Hindawi
Geofluids
Volume 2022, Article ID 7202972, 9 pages
https://doi.org/10.1155/2022/7202972

Research Article

Study on Fluid Front Motion of Water, Nitrogen, and CO_2 during Anisotropic Flow in Shale Reservoirs

Xiangxiang Zhang,[1,2] **Kai Gu**,[1] **Chengyu Liu**,[1,2] **Yangbing Cao**,[1] **J. G. Wang**,[3] **and Feng Gao**[3]

[1]*Zijin School of Geology and Mining, Fuzhou University, Fuzhou 350108, China*
[2]*Research Center of Geological Engineering, Fuzhou University, Fuzhou, Fujian 350116, China*
[3]*State Key Laboratory for Geomechanics and Deep Underground Engineering, China University of Mining and Technology, Xuzhou 221116, China*

Correspondence should be addressed to Chengyu Liu; liuchengyuphd@126.com

Received 12 August 2022; Accepted 24 September 2022; Published 5 December 2022

Academic Editor: Su Shan-Jie

The fluid front motion is an important phenomenon during anisotropic fluid flow in rock engineering. The pore pressure and mechanical responses may be significantly influenced and show an obvious difference near the moving fluid front. However, few studies have been conducted to investigate the front motion of different types of fluids during anisotropic fluid flow. In this work, a numerical model was proposed to detect the front motion of water, nitrogen, and CO_2 in anisotropic shale reservoirs. The full coupling effects among mechanical deformation, fluid flow, and moving boundary in anisotropic porous media were considered in the model construction. The impacts of different fluid properties among water, nitrogen, and CO_2 on the anisotropic fluid flow have been discussed. Then, the proposed model was applied to study the differences in front motion among different types of fluids in anisotropic shales. The impacts of permeability and mobility on fluid front motion were investigated. The theoretical equations for predicting the fluid front motion of different types of fluids were established by introducing corresponding correction coefficients to the previous formulas. The results showed that the model can well describe the anisotropic fluid permeation process. The fluid front motion increased with the increase of permeability and mobility. At the same permeability or mobility, the nitrogen front motion was the largest and the water front motion was the smallest. The difference in fluid front motion among water, nitrogen, and CO_2 was caused by the difference of their viscosity and compressibility. The proposed formulas can fast and accurately predict the evolution of fluid front motion for different types of fluids.

1. Introduction

In engineering practice, fluid permeation through porous media is a very common phenomenon [1–4]. During hydraulic fracturing, the fracturing fluid continues to permeate outward and the seepage boundary keeps moving, resulting in an expanding seepage area [5–8]. According to the effective stress principle, the pore pressure in the seepage area increases and the effective stress in the rock changes, which leads to crack sprouting and expansion and finally to damage [8–11]. Bruno and Nakagawa [12] investigated the effect of pore pressure on fracture evolution in sedimentary rocks and showed that fluid permeation changes the pore pressure distribution, which in turn affects crack propagation. Based on the hydraulic fracturing test with different injection rates, Solberg et al. [13] found that the injection rate had a significant effect on the permeability of the fracturing fluid, which led to changes in rock fracture pressure, crack propagation, and acoustic emission characteristics. Ikeda and Tsukahara [14] studied the effect of pore pressure

on the hydraulic fracture load profile. The results showed that fluid permeation increase the rock pore pressure and leads to the tensile damage around the borehole. Chen et al. [15] found that the hydraulic fracturing mode and crack morphology are related to the permeation characteristics of the fracturing fluid. Based on the pulsating nitrogen fatigue test of low-permeability coal. [16, 17, 18] found that the permeability of the coal was enhanced after fatigue fracturing. Through the comparative tests of hydraulic fracturing and SC-CO_2 fracturing, Zhang et al. [19] showed that the difference in breakdown pressure was due to the difference in fluid front motion and seepage area between water and SC-CO_2. Therefore, the fluid front motion has significant influences on the fracturing mechanism of the rock, which should be carefully considered in fluid-solid coupling analysis.

A series of experiments have been carried out to study the fluid front motion in porous media. According to the change of electrical conductivity, Guizzardi et al. [1] investigated the fluid permeation in porous media and the evolution of penetration depth with time. Khatri and Sirivivatnanon [20] performed the water permeation tests in concrete and establish a theoretical relationship between concrete permeability and penetration depth. In the process of water permeation, the fluid follows Darcy's law at lower injection pressure and obeys the diffusion law at higher injection pressures [21]. The fluid front motion was influenced by injection pressure, injection time, and water-cement ratio [22]. Based on the permeation tests on the Queenston shale using water, bentonite solution, and polymer solution, Al-Maamori et al. [23] found that the type of fluid has a significant effect on the fluid front motion. The permeation tests on concrete with different components and water-cement ratio showed that the fluid front motion was also influenced by the permeation properties of fluid and concrete components as well as fluid types and water-cement ratio [24, 25]. However, most experiments were conducted under 1D simple condition, neglecting rock anisotropy. Meanwhile, the parametric analysis is inevitably limited in experimental research.

In numerical simulation, fluid permeation can be regarded as a moving boundary problem. The size of the permeability domain, the shape of the seepage boundary, and the related parameters and variables must be determined [26, 27]. Several fluid-solid coupling models for two-phase flow have been constructed to study the CO_2 seepage law and its penetration depth in rocks [28–30]. Lockington et al. [31] developed a prediction model based on the seepage equation for unsaturated porous media, and this model was verified by the experimental data. Wang and Ueda [32] considered concrete as a mesoscale three-phase mixture and established a grid network model based on unsaturated seepage theory to investigate the water absorption properties and water penetration depth of concrete. In order to easily determine the fluid front motion, several analytical formulations based on Darcy's law ([20, 22]; and [21]) have been proposed to calculate the penetration depth of incompressible fluids. According to the evolution of fluid front motion with time, Al-Maamori et al. [23] proposed a fitting formula for the penetration depth, in which the fitting parameters were related to fluid type and rock characteristics. Wang et al. [3] deduced a theoretical formula for the fast calculation of the penetration depth of compressible fluid. However, the differences in fluid front motion among incompressible fluid, ideal gas, and real gas have not been well studied. The influences of permeability, viscosity, and rock anisotropy on fluid front motion are still unclear.

In order to study the fluid front motion of different types of fluids, an anisotropic fluid-solid-moving boundary coupling model is established in this study. The rock anisotropy in different physical process is fully considered in model construction. The critical state of CO_2 and the differences in compressibility and viscosity among different types of fluids are considered. This model is applied to study the influences of permeability, mobility, fluid type, and fluid characteristics on the penetration depth of fluid front. A theoretical formula for fast determination of penetration depth is proposed for fluid permeation in anisotropic porous media.

2. Governing Equations for Each Physical Process

2.1. Governing Equation for Anisotropic Deformation. For a pseudostatic deformation process, the equation of motion is [5]

$$G_{\perp} u_{i,kk} + \zeta_j \delta_{ij} u_{k,ki} + \gamma_j \left(\delta_{ij} - \delta_{jk}\right) u_{k,ki} + \alpha p_{,i} + f_i = 0, \quad (1)$$

where $G_{\perp}$ is the shear modulus in the plane vertical to isotropic plane, f_i is the body force per unit volume in the ith direction, p is the pore pressure, $\alpha = 1 - K/K_s$ is the Biot coefficient, K is the bulk modulus of the porous media, K_s is the bulk modulus of grains, ζ_j and γ_j are the rock parameters related to the elastic modulus and Poisson's ratio, and δ_{ij} is the Kronecker delta.

2.2. Porosity and Permeability Model. Shale is a typical porous media, and its porosity can be obtained as [33]

$$\frac{\phi}{\phi_0} = 1 + \left(1 - \frac{\alpha}{\phi_0}\right) \frac{\psi_0 - \psi}{1 + \psi}, \quad (2)$$

where ϕ_0 is the initial porosity and ψ_0 and ψ are the initial and current effective volumetric strains, which are expressed as

$$\psi = \varepsilon_v + \frac{p}{K_s},$$
$$\psi_0 = \varepsilon_{v0} + \frac{p_0}{K_s}, \quad (3)$$

where ε_{v0} and ε_v represent the initial and current volumetric strain, respectively, and p_0 represents the initial pore pressure.

According to Equation (3), the following equation can be derived as

$$\frac{\partial \phi}{\partial t} = \frac{\alpha - \phi}{1 + \psi}\left(\frac{\partial \varepsilon_v}{\partial t} + \frac{1}{K_s}\frac{\partial p}{\partial t}\right). \tag{4}$$

In the anisotropic porous media, the permeability in i th direction is related to the effective strain in jth direction as [5]

$$\frac{k_i}{k_{i0}} = \left[1 + \left(1 + \frac{2(1 - R_j)}{\phi_0}\right)\Delta\varepsilon_{ej}\right]^3, \quad i \neq j, \tag{5}$$

where k_i and k_{i0} are the current and initial permeability in ith direction; $R_j = \triangle\varepsilon_{mj}/\triangle\varepsilon_j$ is the strain proportion of matrix in the jth direction.

2.3. Governing Equation for Anisotropic Fluid Flow. During fluid permeation into anisotropic shale, it obeys the Darcy's law. Thus, the anisotropic fluid flow for water, nitrogen, and CO_2 can be expressed as [2]

$$c_\rho\left[\phi\frac{\partial p}{\partial t} - \frac{k_i}{\mu}(\nabla_i p)^2\right] + \frac{\alpha - \phi}{K_s(1 + \psi)}\frac{\partial p}{\partial t} - \nabla\cdot\left(\frac{k_i}{\mu}\nabla_i p\right) = \frac{\phi - \alpha}{1 + \psi}\frac{\partial \varepsilon_v}{\partial t}, \tag{6}$$

where c_ρ is the isothermal coefficient of compressibility [34]. μ is the dynamic viscosity of fluid.

The density of water is generally considered as constant and $c_\rho = 0$. The density of gas is controlled by the temperature and pressure; thus, $c_\rho = (1/p) - ((1/z)(\partial Z/\partial p))$. Z (dimensionless) is the compressibility factor of real gas.

Nitrogen is usually considered as ideal gas; thus, $Z = 0$ and $c_\rho = 1/p$. For CO_2 under critical temperature, its density and viscosity vary with the pressure, especially near the critical pressure. According to the experimental results, the compressibility factor and viscosity of CO_2 under critical temperature can be expressed by the fitting formulas as [19]

$$Z = A_1 e^{p_r/B_1} + A_2 e^{p_r/B_2} + A_3 p_r + A_4, \tag{7}$$

$$\mu_{CO2} = C_1 e^{p_r/D_1} + C_2 e^{p_r/D_2} + C_3, \tag{8}$$

where A_1~A_4, B_1~B_2, C_1~C_3, and D_1~D_2 are the fitting parameters of CO_2 as shown in Tables 1 and 2, which can be determined by Zhang et al. [2]. According to Equation (7), the isothermal coefficient of compressibility of CO_2 under critical temperature is

$$c_{CO_2} = \frac{1}{p} - \frac{A_1 B_2 e^{p_r/B_1} + A_2 B_1 e^{p_r/B_2} + A_3 B_1 B_2}{p_c B_1 B_2 (A_1 e^{p_r/B_1} + A_2 e^{p_r/B_2} + A_3 p_r + A_4)}. \tag{9}$$

2.4. Moving Boundary Method. The fluid permeation into rock is a typical moving boundary problem with moving fluid boundary and changing permeation zone [35]. Thus, the penetration depth of fluid front should be firstly calculated to determine the computational domain and boundary as shown in Figure 1 [2]. The moving velocity of fluid front can be obtain by Darcy's law as

$$\vec{v}_{bi} = \frac{\partial L_i}{\partial t} = -\frac{k_i}{\mu}\frac{\partial p}{\partial i}\bigg|_{i=L_i}. \tag{10}$$

In general, anisotropy is the most distinctive feature of rock materials, particularly shale formation. Equation (10) can be used to calculate the anisotropic fluid front motion in anisotropic shale. Based on the time integration of moving velocity, the moving fluid boundary and changing permeation zone can be determined by the location of fluid front.

3. Construction of Anisotropic Fluid-Solid-Moving Boundary Coupling Model

According to the above study, the 1D formula is not applicable to predict the penetration depth during 2D fluid permeation. Therefore, an anisotropic fluid-solid-moving boundary coupling model for fluid permeation is established by fully coupling the anisotropic deformation (Equation (1)), the anisotropic fluid flow (Equation (6)), and the moving velocity of fluid front (Equation (10)). Their interactions are shown in Figure 2. Combined with the constitutive model of porosity and permeability (Equations (2) and (5)), this model can solve the fluid front motion in anisotropic shale by COMSOL.

Differences in seepage characteristics and the velocity of movement of seepage boundaries in porous media affect the magnitude and distribution of pore pressure. Therefore, in this section, water, nitrogen, and CO_2 fracturing were used to explore the differences in fluid front motion among uncompressible fluid, ideal gas, and critical temperature fluid in bedding shale. In the numerical simulation, the temperature is set as the critical temperature of CO_2. The viscosities of water and nitrogen are 1 mPa·s and 0.018 mPa·s, respectively. The viscosity of CO_2 is determined by Equation (8), and other main parameters are shown in Table 3.

4. Fluid Front Motion of Water, Nitrogen, and CO_2

Based on the numerical model developed above, this section takes water, nitrogen, and carbon dioxide fracturing as examples to study the factors affecting the penetration depth of incompressible fluid, ideal gas, and critical temperature fluid, such as permeability, viscosity, fluid compressibility, viscosity, and mobility. And then, the prediction equations for the fluid front motion of different types of fluids are established by introducing the corresponding correction functions to the previous formulas.

4.1. Impact of Permeability on Fluid Front Motion. The moving velocity of fluid front is associated with the permeability, so the influence of permeability on penetration depth should be well investigated. In this section, the temperature is set as the critical temperature of CO_2, and the viscosity of water and nitrogen is considered as constant. The viscosity of

Table 1: Parameters for the fitting formula of CO_2 compressibility factor.

	A_1	A_2	A_3	A_4	B_1	B_2
$p < p_c$	-2.61556E-4	-2.8701E-48	-0.43915	1.00157	0.15155	0.00927
$p > p_c$	-3.606	0	0	3.66	-26.704	0

Table 2: Parameters for the fitting formula of CO_2 viscosity.

	C_1	C_2	C_3	D_1	D_2
$p < p_c$	0.04744	0	15.2715	0.2003	0
$p > p_c$	-2.29081E7	-141.52906	186.689	-0.0717	-7.8103

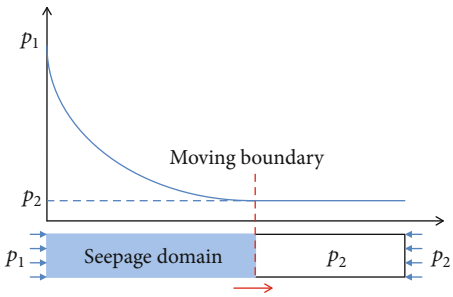

Figure 1: 1D seepage-controlled model with moving boundary.

CO_2 is determined by formula, and the other main parameters are shown in Table 3. Figure 3 represents the variation of penetration depth with permeability for an injection time of 100 h. It shows that the penetration depth of water, nitrogen, and CO_2 increases with the increase of permeability, and the penetration depth evolution curve has typical nonlinear characteristics. At the same permeability, the penetration depth of nitrogen is the largest, and the penetration depth of water is the smallest. The penetration depth of CO_2 is smaller than that of nitrogen, but larger than that of water.

4.2. Pore Pressure Distribution of Different Fluids. When the permeability is $1 \times 10^{-19} m^2$ and the permeability time is 100 h, the pore pressure distribution of water, nitrogen, and CO_2 is shown in Figure 4. It can be seen that before the fluid front extends to the outer boundary, it moves outward in an elliptical shape due to the typical anisotropy of the permeability in bedding shale. The moving fluid front forms an elliptical permeation zone, and the main axis of permeability (x-axis and y-axis) is the symmetry axis of this permeation zone. The pore pressure in the permeation zone decreases along the radial direction, while the pore pressure in the initial state zone remains unchanged. The fluid front also is the dividing line between the permeation zone and the initial state zone. At the same permeation time, the permeation zone of water is the smallest and the permeation zone of nitrogen is the largest. Thus, the permeation zone of CO_2 is smaller than that of nitrogen, but larger than that of water. It shows that the different fluid front motion of different fluids leads to significant difference in the size of the permeation zone and pore pressure distribution.

4.3. Evolution of Compressibility and Viscosity. Figure 5 shows the evolution of pore pressure, compressibility coefficient, and viscosity of water and gas along the y direction. In Figure 5(a), the penetration depth and pore pressure evolution curves of water, nitrogen, and CO_2 are different, which leads to different pore pressure gradients on the fluid front. Thus, the moving velocities of the fluid front for water, nitrogen, and CO_2 are significantly different. In Figure 5(b), the compressibility coefficient of water remains constant, while that of nitrogen increases continuously in the permeation zone and remains constant in the initial state zone. The compressibility coefficient of CO_2 increases slowly in the permeation zone. It increases sharply and then decreases sharply near its critical state, resulting in an obvious peak at the critical state. But the compressibility coefficient of CO_2 in the initial state remains constant. At the same time, the compressibility coefficient of water is the smallest. Before the critical state, the compressibility coefficient of CO_2 is smaller than that of nitrogen. But after the critical state, the compression coefficient of CO_2 becomes larger than that of nitrogen. In Figure 5(c), the viscosity of water and nitrogen remain constant, and the viscosity of water is much higher than that of nitrogen and CO_2. The viscosity of CO_2 in the permeation zone continues to decrease and increase sharply near its critical state, while the viscosity of CO_2 in the initial state remains constant and slightly lower than that of nitrogen. It shows that there are significant differences in pore pressure, compressibility coefficient, and viscosity evolution among different fluids during fluid permeation. Furthermore, according to the Equation (10), the moving velocity of fluid front is determined by permeability, viscosity, and pore pressure gradient, and the pore pressure distribution is closely related to the compressibility and viscosity of the fluid. Therefore, the differences in fluid compressibility and viscosity are the main factor leading to the difference in fluid front motion and pore pressure distribution among water, nitrogen, and CO_2 as shown in Figures 3 and 4.

4.4. Impact of Mobility on Fluid Front Motion. Mobility can characterize the effects of permeability and viscosity on fluid permeation, so it is important to study the difference of water and gas penetration depth with mobility. In this section, the permeability and viscosity of water, nitrogen, and CO_2 used in numerical simulation are shown in Table 4. Since the CO_2 viscosity varies with the pressure, the CO_2 viscosity at the injection pressure is used as the CO_2 viscosity to calculate the mobility. Figure 6 shows the evolution of the penetration depth of water and gas with mobility. It can be seen that even if the viscosity and permeability are different, the penetration depth of

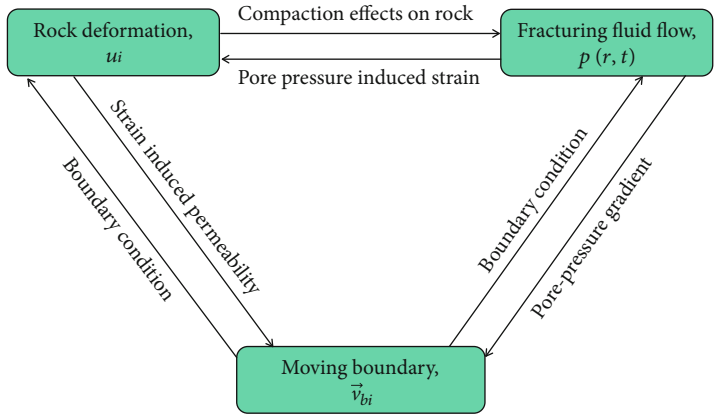

Figure 2: Interaction effect among rock deformation, fracturing fluid flow, and moving boundary method.

Table 3: Computational parameters of bedding shale for numerical simulation.

Parameter	Value
Density of rock, ρ_s (kg/m^3)	2570
Elastic modulus of rock, E (GPa)	$E_x = E_z = 30$, $E_y = 20$
Bulk modulus of grains, K_s (GPa)	60
Poisson's ratio, ν	$\nu_{xy} = 0.2$, $\nu_{yz} = \nu_{xz} = 0.3$
Initial porosity, ϕ_0	0.03
Viscosity of water, μ (mPa·s)	1
Bulk of water, K (GPa)	2
Initial permeability, k_0 (m^2)	$k_{x0} = 5 \times 10^{-18}$, $k_{y0} = 1 \times 10^{-18}$
Initiation pore pressure, p_0 (MPa)	5
Injection pressure, p_I (MPa)	20

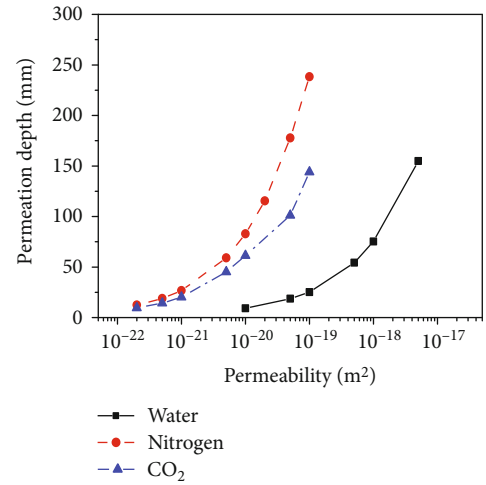

Figure 3: Changes of permeation depth with permeability during water and gas permeation.

nitrogen remains the same with the same mobility, which further shows that mobility can characterize the combined effect of permeability and viscosity. At the same time, the penetration depth of water and gas increases nonlinearly with the increase of mobility. At the same mobility, the penetration depth of CO_2 is the largest, and the penetration depth of water is the smallest. Thus, the penetration depth of nitrogen is larger than that of water, but smaller than that of CO_2. Since the mobility can characterize the combined effect of permeability and viscosity, the main reason for the difference of the penetration depth of water, nitrogen, and CO_2 shown in Figure 6 is their different compressibility. The compressibility will affect the pore pressure distributions of water, nitrogen, and CO_2, resulting in different pore pressure gradients and different moving velocities of fluid front. Therefore, the penetration depths of different fluids are significantly different.

4.5. Theoretical Formulas for Predicting the Penetration Depth. In engineering practice, it is often necessary to quickly estimate the penetration depth of fluids. Wang et al. [3] derived a theoretical formula based on the theory of seepage mechanics, which is expressed as [3]

$$\begin{cases} L_w = \sqrt{2m_f(p_1 - p_0)t}, \\ L_g = \sqrt{m_f \dfrac{{p_1}^2 - {p_0}^2}{p_0} t}. \end{cases} \tag{11}$$

In Equation (10), p_1 and p_0 are the fluid pressure on the seepage boundary, and m_f is the mobility. However, this formula is only suitable for incompressible fluids and ideal gas under one-dimensional conditions. In engineering practice, the permeation processes of water and gas are generally two-dimensional problems. Furthermore, the compressibility and viscosity of CO_2 at critical temperature are obviously different from that of ideal gas. Thus, the penetration depth of nitrogen and CO_2 are significantly different, and the previous formula is not applicable to the situation of this work. The revised equation for predicting the penetration depth of water in bedding shale under two-dimensional condition has been proposed by Zhang et al. [19]. Based on this method, corresponding correction functions were introduced to predict the penetration depth of water, nitrogen, and CO_2 in bedding shale under two-dimensional conditions, which can be obtained as

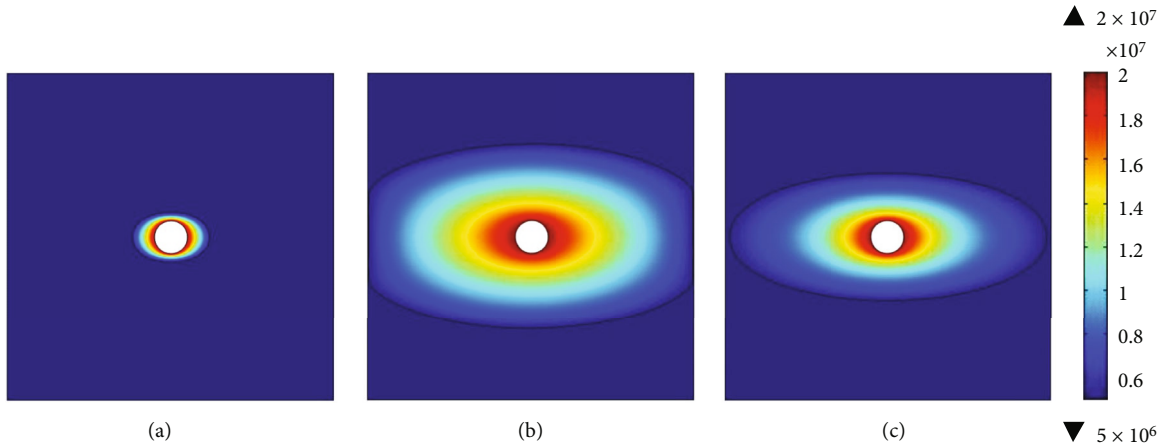

Figure 4: Pore pressure distribution during water and gas permeation: (a) water, (b) nitrogen, and (c) CO_2.

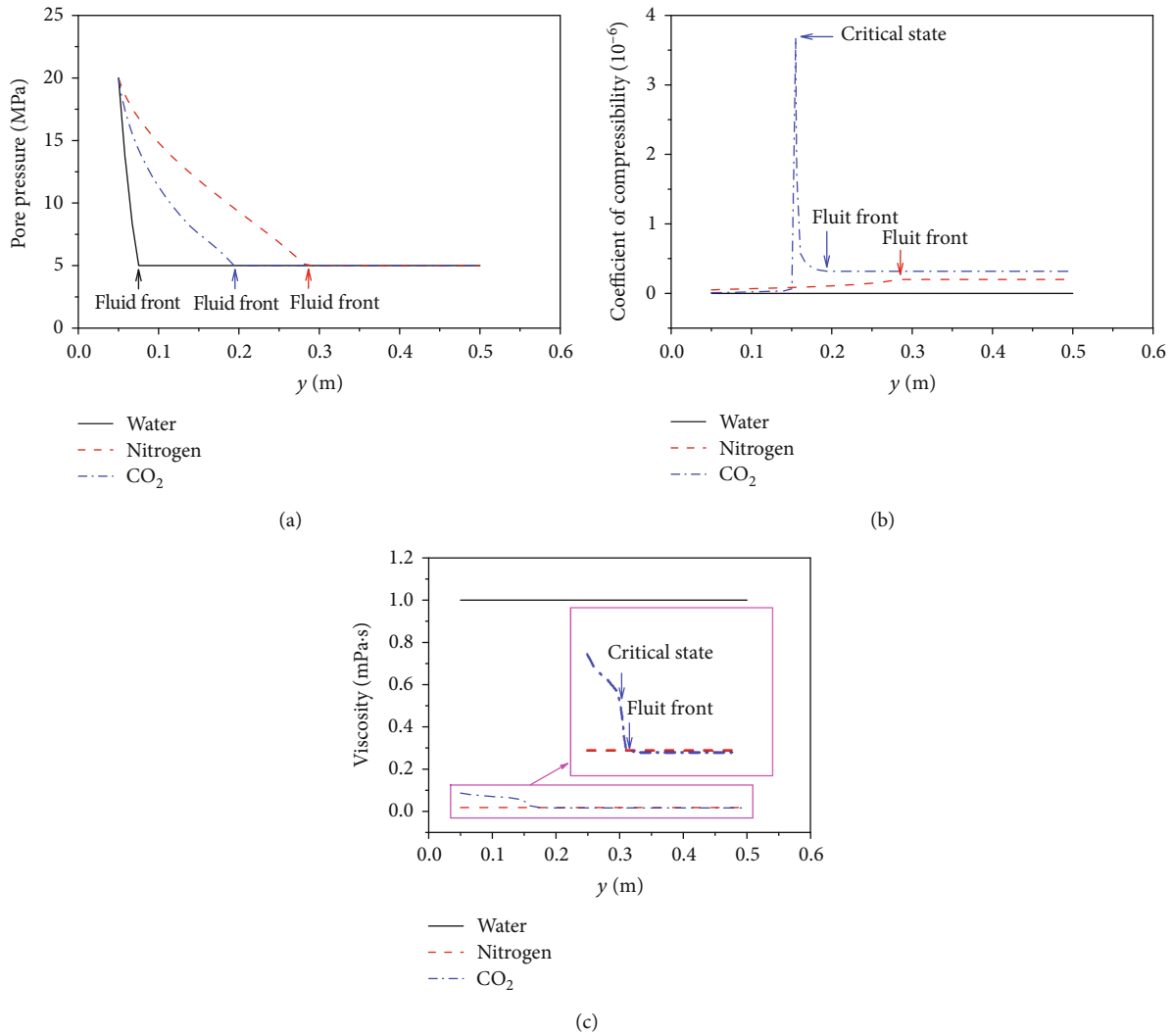

Figure 5: Changes of pore pressure and the coefficient of compressibility and viscosity along the y direction during water and gas permeation.

Table 4: Computational parameters for simulation of water and gas permeation.

Parameter	Water	Nitrogen	CO_2
Initial permeability, k_{y0} (m^2)	$1 \times 10^{-20} \sim 5 \times 10^{-16}$	$2 \times 10^{-22} \sim 1 \times 10^{-19}$	$2 \times 10^{-22} \sim 1 \times 10^{-19}$
Viscosity, μ (mPa·s)	$1 \sim 10^{-2}$	$0.018 \sim 1.8$	0.0867

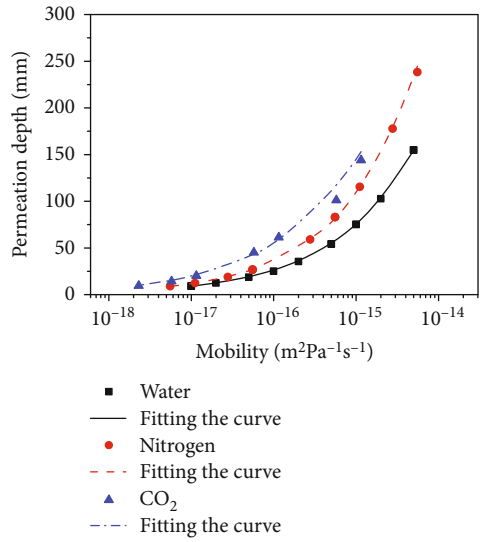

Figure 6: Changes of permeation depth with mobility during water and gas permeation.

$$\begin{cases} L_{wr} = f_w \sqrt{2m_f(p_1 - p_0)t}, \\ L_{nr} = f_n \sqrt{m_f \dfrac{{p_1}^2 - {p_0}^2}{p_0} t}, \\ L_{cr} = f_c \sqrt{m_f \dfrac{{p_1}^2 - {p_0}^2}{p_0} t}. \end{cases} \tag{12}$$

In Equation (12), f_w, f_n, and f_c are the corresponding correction functions of water, nitrogen, and CO_2, respectively. They can be calculated by the nonlinear fitting of the numerical simulation results. According to the simulation results in Figure 6, the correction functions in Equation (12) can be obtained as

$$\begin{cases} f_w = -0.072 \lg m_f - 0.365, \\ f_n = -0.027 \lg m_f + 0.247, \\ f_c = -0.150 \lg m_f - 0.373. \end{cases} \tag{13}$$

It can be seen that the prediction results of the formula are in good agreement with the simulation results, indicating that the improved theoretical formula proposed in this section can accurately predict the penetration depth of water, nitrogen, and CO_2 in bedding shale.

5. Conclusions

In this study, the differences in compressibility and viscosity among incompressible fluid, ideal gas and critical temperature fluid, and the fluid front motion in bedding shale were seriously considered. The rock anisotropy in different physical processes was analyzed during model construction, and the critical state of CO_2 was seriously discussed. The proposed model in this work was used to study the influences of permeability, mobility, fluid type, and fluid characteristics on the penetration depth of fluid front. The differences of fluid front motion among water, nitrogen, and CO_2 were compared, and its internal mechanisms were analyzed. Corresponding improved formulas for rapid prediction of water, nitrogen, and CO_2 penetration depth were proposed. The main conclusions and findings are summarized as below.

Firstly, an anisotropic fluid-solid-moving boundary coupling model for bedding shale was established to describe the permeation process of different fluids. This model considered the anisotropy of deformation, fluid flow, and fluid front motion in bedding shale. The differences in compressibility and viscosity among incompressible fluid, ideal gas, and critical temperature fluid were analyzed. The moving boundary algorithm was coupled to describe the movement law of fluid permeability boundary.

Secondly, the effects of permeability, compressibility, viscosity, mobility, and fluids on penetration depth were investigated. The results showed that the penetration depth increases with the increase of permeability. When the mobility was the same, the penetration depth remained the same even if the permeability and viscosity were different. The penetration depth increased with the also increase of mobility.

Thirdly, the differences in permeation boundary motion among water, nitrogen, and CO_2 were comparatively analyzed. A rapid method to predict the penetration depth was proposed. The results showed that the penetration depth of water was the smallest at the same permeability or mobility, while the penetration depth of nitrogen was larger than that of CO_2 at the same permeability. However, the penetration depth of nitrogen was smaller than that of CO_2 under the same mobility. The main reason for these differences in penetration depth was the different evolution laws of compressibility and viscosity among water, nitrogen, and CO_2. In order to fast calculate the penetration depth, new theoretical formulas were established to predict the penetration depth of water, nitrogen, and CO by introducing the correction functions to the previous formulas. The correction functions were related to mobility. The effectiveness of the proposed formulas was verified through simulation results.

Data Availability

The data used to support the findings of this study are available from the corresponding author upon request after this paper is published.

Conflicts of Interest

The authors declare that they have no conflicts of interest.

Acknowledgments

The authors are grateful to the financial support from the Natural Science Foundation of Fujian Province of China (Grant No. 2020J05133), the Young and Middle-Aged Education Research Project of Fujian Provincial Education Department (Grant No. JAT190052), and the National Natural Science Foundation of China (Grant No. 42202301).

References

[1] M. Guizzardi, D. Derome, D. Mannes, R. Vonbank, and J. Carmeliet, "Electrical conductivity sensors for water penetration monitoring in building masonry materials," *Materials and Structures*, vol. 49, no. 7, pp. 2535–2547, 2016.

[2] X. Zhang, Y. Lu, J. Tang, Z. Zhou, and Y. Liao, "Experimental study on fracture initiation and propagation in shale using supercritical carbon dioxide fracturing," *Fuel*, vol. 190, pp. 370–378, 2017.

[3] J. G. Wang, Y. Ju, F. Gao, and J. Liu, "A simple approach for the estimation of CO_2 penetration depth into a caprock layer," *Journal of Rock Mechanics and Geotechnical Engineering*, vol. 8, no. 1, pp. 75–86, 2016.

[4] X. Zhou and T. J. Burbey, "Fluid effect on hydraulic fracture propagation behavior: a comparison between water and supercritical CO_2-like fluid," *Geofluids*, vol. 14, 188 pages, 2014.

[5] X. Zhang, J. G. Wang, X. Wang, and F. Gao, "Numerical performances of invariable and moving boundary methods during fluid penetration into anisotropic porous media," *Computers and Geotechnics*, vol. 121, article 103458, 2020.

[6] T. Liang, L. Shao, E. Yao et al., "Study on fluid-rock interaction and reuse of flowback fluid for gel fracturing in desert area," *Geofluids*, vol. 2018, Article ID 8948961, 9 pages, 2018.

[7] Z. Bennour, T. Ishida, Y. Nagaya et al., "Crack extension in hydraulic fracturing of shale cores using viscous oil, water, and liquid carbon dioxide," *Rock Mechanics and Rock Engineering*, vol. 48, no. 4, pp. 1463–1473, 2015.

[8] J. Zhou, Y. Jin, and M. Chen, "Experimental investigation of hydraulic fracturing in random naturally fractured blocks," *International Journal of Rock Mechanics and Mining Sciences*, vol. 47, no. 7, pp. 1193–1199, 2010.

[9] M. Chen, C. Zang, Z. Ding et al., "Effects of confining pressure on deformation failure behavior of jointed rock," *Journal of Central South University*, vol. 29, no. 4, pp. 1305–1319, 2022.

[10] Z. P. Bažant, M. Salviato, V. T. Chau, H. Viswanathan, and A. Zubelewicz, "Why fracking works," *Journal of Applied Mechanics*, vol. 81, no. 10, article 101010, 2014.

[11] I. Matsunaga, H. Kobayashi, S. Sasaki, and T. Ishida, "Studying hydraulic fracturing mechanism by laboratory experiments with acoustic emission monitoring," *International Journal of Rock Mechanics & Mining Sciences & Geomechanics Abstracts*, vol. 30, no. 7, pp. 909–912, 1993.

[12] M. S. Bruno and F. M. Nakagawa, "Pore pressure influence on tensile fracture propagation in sedimentary rock," *International journal of rock mechanics and mining sciences & geomechanics abstracts*, vol. 28, no. 4, pp. 261–273, 1991.

[13] P. Solberg, D. Lockner, and J. D. Byerlee, "Hydraulic fracturing in granite under geothermal conditions," *International Journal of Rock Mechanics and Mining Sciences & Geomechanics Abstracts*, vol. 17, no. 1, pp. 25–33, 1980.

[14] R. Ikeda and H. Tsukahara, "Hydraulic fracturing technique: pore pressure effect and stress heterogeneity," *International Journal of Rock Mechanics and Mining Sciences & Geomechanics Abstracts*, vol. 26, no. 6, pp. 471–475, 1989.

[15] Y. Chen, Y. Nagaya, and T. Ishida, "Observations of fractures induced by hydraulic fracturing in anisotropic granite," *Rock Mechanics and Rock Engineering*, vol. 48, no. 4, pp. 1455–1461, 2015.

[16] E. Fjar, R. M. Holt, A. M. Raaen, P. Horsrud, A. M. Raaen, and R. Risnes, *Petroleum Related Rock Mechanics*, Elsevier, 2008.

[17] Y. Xue, J. Liu, P. G. Ranjith, F. Gao, H. Xie, and J. Wang, "Changes in microstructure and mechanical properties of low-permeability coal induced by pulsating nitrogen fatigue fracturing tests," *Rock Mechanics and Rock Engineering*, 2022.

[18] Y. Xue, P. G. Ranjith, Y. Chen, C. Cai, F. Gao, and X. Liu, "Nonlinear mechanical characteristics and damage constitutive model of coal under CO_2 adsorption during geological sequestration," *Fuel*, vol. 331, p. 125690, 2023.

[19] X. Zhang, J. G. Wang, F. Gao, and Y. Ju, "Impact of water, nitrogen and CO_2 fracturing fluids on fracturing initiation pressure and flow pattern in anisotropic shale reservoirs," *Journal of Natural Gas Science and Engineering*, vol. 45, pp. 291–306, 2017.

[20] R. P. Khatri and V. Sirivivatnanon, "Methods for the determination of water permeability of concrete," *Materials Journal*, vol. 94, no. 3, pp. 257–261, 1997.

[21] J. H. Yoo, H. S. Lee, and M. A. Ismail, "An analytical study on the water penetration and diffusion into concrete under water pressure," *Construction and Building Materials*, vol. 25, no. 1, pp. 99–108, 2011.

[22] J. Murata, Y. Ogihara, S. Koshikawa, and Y. Itoh, "Study on watertightness of concrete," *Materials Journal*, vol. 101, no. 2, pp. 107–116, 2004.

[23] H. M. S. Al-Maamori, M. H. El Naggar, and S. Micic, "Depth of penetration of lubricant fluids and water in Queenston shale of southern Ontario," *Canadian Geotechnical Journal*, vol. 54, no. 2, pp. 248–257, 2017.

[24] K. S. Chia and M. Zhang, "Water permeability and chloride penetrability of high-strength lightweight aggregate concrete," *Cement and Concrete Research*, vol. 32, no. 4, pp. 639–645, 2002.

[25] X. Liu, K. S. Chia, and M. Zhang, "Water absorption, permeability, and resistance to chloride-ion penetration of lightweight aggregate concrete," *Construction and Building Materials*, vol. 25, no. 1, pp. 335–343, 2011.

[26] K. N. Christodoulou and L. E. Scriven, "Discretization of free surface flows and other moving boundary problems," *Journal of Computational Physics*, vol. 99, no. 1, pp. 39–55, 1992.

[27] P. A. Sackinger, P. R. Schunk, and R. R. Rao, "A Newton–Raphson pseudo-solid domain mapping technique for free and moving boundary problems: a finite element

implementation," *Journal of Computational Physics*, vol. 125, no. 1, pp. 83–103, 1996.

[28] J. G. Wang and Y. Peng, "Numerical modeling for the combined effects of two-phase flow, deformation, gas diffusion and CO_2 sorption on caprock sealing efficiency," *Journal of Geochemical Exploration*, vol. 144, pp. 154–167, 2014.

[29] L. K. Abidoye, K. J. Khudaida, and D. B. Das, "Geological carbon sequestration in the context of twophase flow in porous media: a review," *Critical Reviews in Environmental Science and Technology*, vol. 45, no. 11, pp. 1105–1147, 2015.

[30] Y. Dai, Z. Zhou, J. Lin, and J. Han, "Modeling of two-phase flow in rough-walled fracture using level set method," *Geofluids*, vol. 2017, Article ID 2429796, 11 pages, 2017.

[31] D. Lockington, J. Y. Parlange, and P. Dux, "Sorptivity and the estimation of water penetration into unsaturated concrete," *Materials and Structures*, vol. 32, no. 5, pp. 342–347, 1999.

[32] L. Wang and T. Ueda, "Mesoscale modeling of water penetration into concrete by capillary absorption," *Ocean Engineering*, vol. 38, no. 4, pp. 519–528, 2011.

[33] H. Zhang, J. Liu, and D. Elsworth, "How sorption-induced matrix deformation affects gas flow in coal seams: a new FE model," *International Journal of Rock Mechanics and Mining Sciences*, vol. 45, no. 8, pp. 1226–1236, 2008.

[34] F. Civan, C. S. Rai, and C. H. Sondergeld, "Shale-gas permeability and diffusivity inferred by improved formulation of relevant retention and transport mechanisms," *Transport in Porous Media*, vol. 86, no. 3, pp. 925–944, 2011.

[35] H. Shimizu, S. Murata, and T. Ishida, "The distinct element analysis for hydraulic fracturing in hard rock considering fluid viscosity and particle size distribution," *International Journal of Rock Mechanics and Mining Sciences*, vol. 48, no. 5, pp. 712–727, 2011.